

FASTAR - II. Semi-resolved evolutionary stellar population models

Ignacio Martín-Navarro^{1,2}, Alexandre Vazdekis^{1,2}, Luis Peralta de Arriba³, Isaac Alonso Asensio^{1,2}, Patricia Iglesias Navarro^{1,2}, Eirini Angeloudi^{1,2}, Francesco La Barbera⁴, Miguel Cerviño⁵, Katja Fahrion⁶, Tereza Jerabkova⁷, Michael A. Beasley^{1,2,8}, Jesús Falcón-Barroso^{1,2}, Marc Huertas-Company^{1,2,9,10}, Sebastián F. Sánchez^{11,1,2}, Prashin Jethwa⁵

¹ Instituto de Astrofísica de Canarias, c/ Vía Láctea s/n, E38205 - La Laguna, Tenerife, Spain
e-mail: imartin@iac.es

² Departamento de Astrofísica, Universidad de La Laguna, E-38205 La Laguna, Tenerife, Spain

³ Departamento de Inteligencia Artificial, Universidad Nacional de Educación a Distancia (UNED), Calle Juan del Rosal 16, E-28040 Madrid, Spain

⁴ INAF-Osservatorio Astronomico di Capodimonte, sal. Moiarriello 16, Napoli 80131, Italy

⁵ Centro de Astrobiología (CSIC/INTA), 28692 ESAC Campus, Villanueva de la Cañada, Madrid, Spain

⁶ Department of Astrophysics, University of Vienna, Türkenschanzstraße 17, 1180 Wien, Austria

⁷ Centre for Astrophysics and Supercomputing, Swinburne University, John Street, Hawthorn, VIC 3122, Australia

⁸ Department of Theoretical Physics and Astrophysics, Faculty of Science, Masaryk University, Kotlářská 2, Brno 611 37, Czech Republic

⁹ Observatoire de Paris, LERMA, PSL University, 61 avenue de l'Observatoire, F-75014 Paris, France

¹⁰ Université Paris-Cité, 5 Rue Thomas Mann, 75014 Paris, France

¹¹ Instituto de Astronomía, Universidad Nacional Autónoma de México, A.P. 106, Ensenada 22800, BC, México

Received; accepted

ABSTRACT

Standard evolutionary synthesis models rely on the assumption of a fully sampled stellar initial mass function (IMF). Under this assumption, the age, chemical composition, and IMF uniquely define the predicted absorption spectra. However, with current instrumentation pushing observations towards higher spatial resolutions and lower surface brightnesses, the assumption of a fully sampled IMF does not always hold true. Here we present the semi-resolved version of the FASTAR models, a comprehensive set of evolutionary synthesis predictions able to reproduce the stochastic behavior of discretely-sampled IMFs. Semi-resolved FASTAR predictions share the same evolutionary principles, ingredients, and features of the integral (fully sampled IMF) version of the FASTAR models, expanding a range of ages from 20 Myr to 14 Gyr, metallicities between $-2.5 \leq [M/H] \leq +0.3$, and several IMF functional forms. Detailed spectroscopic measurements can be carried out within the 3,540–7,400 Å wavelength range, and low-resolution spectral energy distributions can also be synthesized over a wider 2,000-to-12,000 Å coverage. Semi-resolved FASTAR models also depend on the number of stars contributing to the observed spectra, which determines the effective sampling of the different stellar evolutionary phases along the isochrones. This incomplete sampling implies that semi-resolved FASTAR models are inevitably stochastic. On top of the inherent stochasticity of the models, derived quantities such as equivalent widths, colors, or mass-to-light ratios might present strong deviations compared to standard fully sampled simple stellar population models. This stochasticity dilutes the boundary between model predictions and data, promoting new sampling-based inference approaches. FASTAR semi-resolved models allow for the effective exploration of the parameter space thanks to their optimized, JAX-based computation.

Key words. galaxies: evolution – galaxies: stellar content – stars: evolution

1. Introduction

Understanding the formation and evolution of galaxies requires an accurate interpretation of their integrated light. Beyond the Local Group, where stars can be individually resolved, the photometric and spectroscopic properties of galaxies are commonly interpreted in terms of physically meaningful quantities via evolutionary stellar population synthesis models. While alternative approaches are possible (e.g., Spinrad & Taylor 1971; Faber 1972; Pickles 1985; Bica & Alloin 1986; Bica 1988; Schmidt et al. 1991; Pelat 1998; Martín-Navarro & Vazdekis 2024) the synthesis of integrated stellar population models anchored in the predictions from stellar evolution theory is now one of the most widely adopted tools in extragalactic astronomy (e.g., Tinsley & Gunn 1976; Worthey 1994; Leitherer et al. 1999; Bruzual & Charlot 2003; Thomas et al.

2003; Maraston 2005; Schiavon 2007; Vazdekis et al. 2010; Conroy & van Dokkum 2012; Robotham & Bellstedt 2025).

Simple stellar population (SSP) models are the fundamental output of evolutionary synthesis codes. An SSP model aims to represent the flux (luminosity) emitted by an (infinitely large) collection of stars with the same age and chemical composition. With the relative number of stars with different masses determined by the stellar initial mass function (IMF), the predicted spectral energy distribution of an SSP model is uniquely defined by the age of the population, its chemistry, and the underlying IMF. Conversely, the observed spectro-photometric properties of galaxies can be translated into these basic parameters or related quantities such as stellar masses or star formation rates (see e.g., Conroy 2013, for an in-depth review of the synthesis and potential uses of evolutionary models).

Over the years, the refinement of SSP models has reached a great level of maturity, and their success is undeniable. Yet, their range of applicability is limited to situations where the fundamental assumptions of evolutionary synthesis hold. While this is true in a large fraction of real-world applications, some interesting astrophysical cases push standard SSP models beyond their limits. In particular, when the number of stars per resolution element (i.e., the number of stars contributing to the observed spectral energy distribution) is not large enough, evolutionary population synthesis becomes intrinsically stochastic (e.g., [Cerviño & Luridiana 2004, 2006](#); [Cerviño 2013](#)). Therefore, in this so-called semi-resolved regime, model predictions are no longer uniquely defined by the age, chemical composition, and IMF of the stellar population.

The stochastic nature of finitely samples stellar populations is well known (e.g., [Buzzoni 1993](#); [Renzini 1998](#); [Cerviño et al. 2002](#); [Conroy & van Dokkum 2016](#)). From a practical perspective, it has mostly been applied to young stellar populations in which the presence or absence of a few massive stars can significantly affect the integrated stellar spectrum of a population (e.g., [da Silva et al. 2012](#); [Eldridge 2012](#); [Krumholz et al. 2015](#); [Orozco-Duarte et al. 2022](#); [Stanway & Eldridge 2023](#)). In addition, the stochasticity in the integrated light of star clusters has also been the subject of dedicated studies ([Cerviño et al. 2000](#); [Bruzual A. 2002](#); [Fouesneau & Lançon 2010](#); [Fouesneau et al. 2012](#); [Beerman et al. 2012](#); [Branco et al. 2024](#)). Moreover, the underlying physical process enabling the use of surface brightness fluctuations as distance ([Tonry & Schneider 1988](#); [Tonry et al. 2001](#); [Blakeslee et al. 2009](#)) and stellar population content ([Cerviño et al. 2008](#); [Rodríguez-Beltrán et al. 2021](#)) indicators is also the inherently stochastic nature of semi-resolved populations.

Semi-resolved stellar populations are therefore a natural expectation. Up until recently, however, the study of them has been focused on the specific scientific cases described above, although current technological advances are pushing the limits out to where stochasticity cannot be neglected. For example, high spatial resolution studies of relatively nearby galaxies using integral field spectroscopy show fluctuations in the recovered stellar population maps larger than expected from the signal-to-noise of the data (e.g., [Pinna et al. 2019](#); [Bittner et al. 2020](#); [Neumann et al. 2020](#); [Martín-Navarro et al. 2021](#); [Drory et al. 2024](#); [Sánchez et al. 2025](#)).

More critically, the increasing sensitivity of optical detectors is pushing the limits of low-surface-brightness studies (e.g., [Abraham & van Dokkum 2014](#); [van Dokkum et al. 2015](#); [Trujillo & Fliri 2016](#); [Mihos et al. 2017](#); [Trujillo et al. 2021](#); [Martínez-Delgado et al. 2025](#)). With forthcoming ground- and space-based facilities specifically devoted to obtaining unprecedentedly deep photometric data, such as the Dark Energy Spectroscopic Instrument ([Dey et al. 2019](#)), Euclid ([Euclid Collaboration et al. 2025, 2026](#)), or the Vera C. Rubin Observatory ([Ivezić et al. 2019](#); [Martin et al. 2022](#)), establishing robust methods to model and interpret semi-resolved observations will be crucial for fully exploiting the scientific potential of the low-surface-brightness Universe. Yet the most important challenge for standard stellar population models lies ahead. The milliarcsecond physical-scale resolution of the next generation of 40-meter-class telescopes, such as the Extremely Large Telescope, will yield semi-resolved observations of every nearby galaxy. In this context, detailed observational astronomy in the coming decades will be, by necessity, semi-resolved.

In the first paper of this series, we presented FASTAR, a differentiable evolutionary stellar population synthesis code. Here

we make use of the fast and optimized tools of FASTAR to describe the synthesis of semi-resolved predictions. These predictions are based on the exact same principles as standard SSP models, retaining their strength and applicability, but are made to match semi-resolved observations with a variable number of stars. The layout of this paper is as follows. In Sect. 2 we detail the basic FASTAR ingredients, in Sect. 3 we present the synthesis of the semi-resolved predictions, and in Sect. 4 we outline the overall behavior of the models. In Sect. 5 we expand on some immediate applications of the FASTAR predictions, while in Sect. 6 we discuss some of the observational practicalities. Finally, in Sect. 7 we summarize the main features of the semi-resolved FASTAR models and outline upcoming developments.

2. Model ingredients

FASTAR semi-resolved predictions are based on the same model ingredients as the standard fully sampled SSP models described in the first paper of this series. Semi-resolved predictions are also computed using the JAX Python library ([Bradbury et al. 2018](#); [Frostig et al. 2019](#)), with native numerical autodifferentiation and optimized computation with both a CPU and GPU. The five main FASTAR ingredients are described in the following.

2.1. Initial mass functions

FASTAR comes with six predefined functional forms for the IMF. Models with both [Kroupa \(2001\)](#) and [Chabrier \(2003\)](#) IMF shapes can be synthesized representing the Milky Way standard. In addition, FASTAR also incorporates a single and a broken power-law (three segments) IMF parameterization with variable slopes. Furthermore, the so-called bimodal IMF functional form described in [Vazdekis et al. \(1996\)](#) is also included as well as a tapered power-law, as defined in [De Marchi et al. \(2005\)](#). All the fixed and variable parameters of these IMF functional forms are easily accessible and modified according to the user's needs. More details on each IMF description are given in Section 2.1 of the first FASTAR paper. In addition to these predefined IMF parametrizations, FASTAR also offers the possibility of generating model predictions for any user-defined IMF functional form.

2.2. Isochrones

Stellar evolutionary theory is coded into the FASTAR models through the BaSTI-IAC isochrones ([Hidalgo et al. 2018](#); [Pietrinferni et al. 2021, 2024](#)). In particular, we used the latest version of their solar-scaled isochrones, including improved prescriptions for atomic diffusion and overshooting. This set of isochrones covers a range in age from 20 Myr to 14 Gyr and -2.5 to +0.3 in total metallicity [M/H], which in practice sets the applicability range of the models.

Currently, FASTAR model predictions do not include variable elemental abundances, even if individual stars have non-solar abundances (see details below in the stellar libraries). As for the case of the standard FASTAR SSP predictions, semi-resolved FASTAR models can be evaluated at any specific age, metallicity, and IMF thanks to the consistent sampling of the BaSTI isochrones.

2.3. Bolometric corrections

Rather than using the bolometric luminosities of the BaSTI-IAC isochrones, we followed the synthesis approach of the MILES

models (Vazdekis et al. 2010, 2015). In this approach, theoretical stellar luminosities are translated into V-band absolute magnitudes using the bolometric corrections of Worthey & Lee (2011). FASTAR predictions are anchored to the Sun, assuming a bolometric magnitude of 4.70 and a V-band bolometric correction of $BC_{\odot} = -0.12$. This results in flux predictions scaled to a distance of 10 parsecs.

2.4. Stellar interpolator

The core component of FASTAR is its stellar interpolator which provides fast, accurate, and differentiable stellar spectra. In a nutshell, FASTAR interpolation follows a similar approach as in Alsing et al. (2020). Instead of predicting the entire spectrum of a star given its atmospheric parameters (T_{eff} , $\log g$, $[\text{Fe}/\text{H}]$), we first reduce the dimensionality of the spectra using a simple principal component analysis (PCA) decomposition. This initial step reversibly compresses the entire spectrum (usually evaluated at a few thousand wavelengths) into, in our case, a 16-element vector, containing the PCA projection coefficients.

Then, a simple fully connected neural network with four hidden layers (64, 128, 128, 64) is trained using a mean squared error loss function to predict these 16 coefficients given the three atmospheric parameters. As demonstrated in the first FASTAR paper, this interpolation scheme performs at the same level as the stellar interpolator behind the MILES models. However, it is orders of magnitude faster in the synthesis of new stellar spectra.

2.5. Stellar libraries

Using the ingredient above, FASTAR can produce two sets of predictions. On the one hand, over the 3,540–7,400 Å wavelength range, FASTAR provides detailed spectroscopic predictions at a 2.51 Å full width at half maximum resolution (same as MILES Falcón-Barroso et al. 2011). These predictions are based on the combination of two stellar libraries: the Medium-resolution Isaac Newton Telescope library of empirical spectra (MILES, Sánchez-Blázquez et al. 2006) and the BOSZ synthetic stellar spectral library (Mészáros et al. 2024). Details on the combination and training of the PCA-based neural network regressor are given in the first FASTAR paper, where we also demonstrate how the combination of both stellar libraries yields accurate stellar predictions across the entire $T_{\text{eff}}-\log g-[\text{Fe}/\text{H}]$ parameter space. Powered by the thoroughly tested MILES stellar templates, this set of FASTAR predictions is meant to be used for detailed spectroscopic analyses.

For many photometric applications, however, a broader wavelength range is required. Therefore, FASTAR has an additional set of predictions that is entirely based on the BOSZ theoretical stellar templates, expanding from 2,000 to 12,000 Å. These alternative FASTAR models can be convolved with any set of photometric filters to reproduce generic spectral energy distributions but are intentionally undersampled in the spectral direction ($\Delta\lambda = 4 \text{ \AA}$) to discourage their use for spectroscopic purposes.

3. Semi-resolved versus integral synthesis

In general, standard evolutionary stellar population models define the flux emitted by an SSP with a given age and metallicity as

$$F_{\lambda}(\text{age}, [\text{M}/\text{H}]) = \int_{m_{\text{low}}}^{m_{\text{high}}(\text{age})} S_{\lambda}^{M_V}(m | \text{age}, [\text{M}/\text{H}]) \chi(m) dm \quad (1)$$

where $S_{\lambda}^{M_V}(m | \text{age}, [\text{M}/\text{H}])$ are the interpolated stellar spectra (scaled to their expected V-band absolute magnitude) and $\chi(m)$ the relative number of stars with different stellar masses, i.e., the IMF. Underneath Eq. 1, stellar evolution theory determines the integration limits (in particular the most massive star contributing to the observed flux), the mapping between stellar mass, age, metallicity and $T_{\text{eff}}-\log g$ (i.e., the isochrones) and the luminosity or scaling factor of each $S_{\lambda}^{M_V}$.

Equation 1, however, only holds valid in the limit where a large enough number of stars are observed within a given resolution element¹. To generate evolutionary semi-resolved predictions, f_{λ} , in FASTAR we modeled the flux of a finite ensemble of stars using a simple summation:

$$f_{\lambda}(\text{age}, [\text{M}/\text{H}], N_{\text{stars}}) = \sum_{i=1}^{N_{\text{stars}}} S_{\lambda}^{M_V}(m | \text{age}, [\text{M}/\text{H}]). \quad (2)$$

Similarly to standard SSP models, stellar evolution theory determines the relation between stellar mass and atmospheric parameters for a given age and metallicity and thus the stellar spectra ($S_{\lambda}^{M_V}$) on the right-hand side of Eq. 2. These stellar spectra are again scaled to match the V-band absolute magnitude predicted by the isochrones (modulo the bolometric correction). The main difference between the integral synthesis (Eq. 1) and the semi-resolved version (Eq. 2) is that in the latter, the mass of each of the N_{stars} is randomly sampled following the assumed IMF.

To illustrate the similarities and differences between integrated and semi-resolved FASTAR predictions, Fig. 1 shows the effect of increasing the number of stars, from 10 to 10,000,000, in an integrated stellar population. In FASTAR, the semi-resolved regime inherits exactly the same stellar population parameters as the standard integrated SSP models, namely age, total metallicity, and IMF, as these quantities define the evolutionary side of the model. On top of these, semi-resolved predictions in FASTAR are characterized by an additional parameter: the number of stars contributing to the integrated flux.

Although the age, metallicity, IMF, and number of stars fully specify the physical model, semi-resolved FASTAR predictions remain stochastic by construction. In other words, a fixed tuple of model parameters (age, $[\text{M}/\text{H}]$, IMF, N_{stars}) does not generate a unique spectrum since the IMF, and thus stellar evolutionary phases, are stochastically sampled. This is the fundamental distinction with respect to standard fully sampled evolutionary synthesis models: while the underlying physics and ingredients are identical, semi-resolved models produce a distribution of possible spectroscopic predictions rather than a single deterministic one.

An important consideration is worth highlighting here. For a given age and metallicity, stellar mass maps stellar evolution in a mono-parametric way, thus defining the properties of the individual stellar spectra that go into the synthesis of an SSP and their luminosities. Therefore, although FASTAR models are calculated through a random mass sampling of the IMF, the synthesized spectra effectively depend on the different stellar evolutionary phases probed by the isochrone. In simpler terms, the

¹ In the optical range, $N_{\text{stars}} \sim 10^5$ typically separates fully sampled from semi-resolved regimes (see e.g., Cerviño & Luridiana 2004, and sections below).

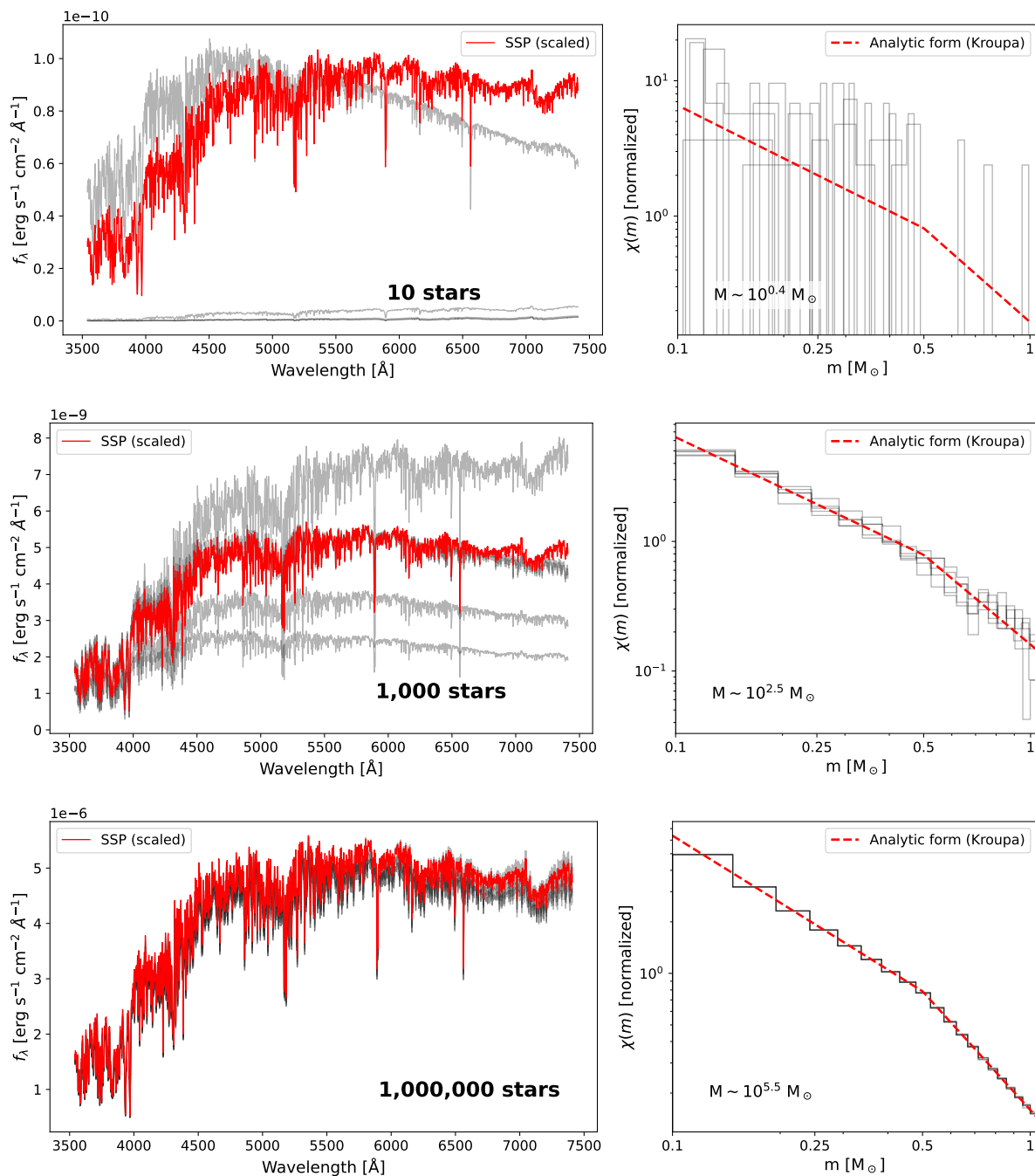


Fig. 1: Stochastic nature of FASTAR semi-resolved predictions. In the left panel, each row shows five random semi-resolved SSP models (in gray) resulting from different stochastic samplings of the IMF. The corresponding IMF realizations are shown in the right panels (also in gray), along with the assumed IMF (red) and the mean stellar mass of the population. For reference, the standard fully sampled SSP prediction is included in red in the left panels (scaled to arbitrary units for comparison). All realizations correspond to a 10 Gyr, solar-metallicity population. From top to bottom, the number of stars increases from 10 to 1,000,000.

presence of a luminous red giant will have a much more noticeable impact on a semi-resolved SSP model than the absence of a low-mass M dwarf. Thus, the variety of spectral properties in the semi-resolved regime results from a complex and nonlinear interaction between the number of stars, their stellar masses, and their evolutionary phase, all of this modulated by the assumed IMF. The upcoming sections will expand on this connection between number of stars, IMF sampling and stellar evolutionary phases.

The intrinsic stochasticity of these models can be quantified in different ways, for instance, by providing the mean spectrum (i.e. the SSP) and its variance for a grid of ages and metallicities (Vazdekis et al. 2020). However, FASTAR offers a more natural approach to modeling the light from semi-resolved populations by explicitly sampling the IMF as many times as needed (N_{stars}) to reproduce the observed data. Note that semi-resolved FASTAR models converge to the fully sampled IMF predictions as

$N_{\text{stars}} \rightarrow \infty$, generalizing the use of evolutionary stellar population models.

Two immediate things are evident from Fig. 1. First, the most obvious one, the scatter decreases as the number of stars increases. It is worth noting also that, as expected, the convergence towards the mean SSP value (red spectra) happens faster towards bluer wavelengths at these old ages (see e.g., Cerviño 2013). Second, on average, the total luminosity increases as well with the number of stars. Contrary to standard fully sampled predictions that are usually scaled to one solar mass, semi-resolved FASTAR models predict the actual flux, scaled at 10 pc, expected from a population with the given number of stars and IMF sampling.

4. Model predictions

Despite the differences between fully sampled and semi-resolved evolutionary model synthesis, the predicted quantities are the same. In particular, FASTAR semi-resolved models can be used to generate spectra as demonstrated in Fig. 1, which can then be analyzed through line-strength indices and colors as traditional models. In addition, mass-to-light ratios can also be retrieved for each realization for any filter within the FASTAR wavelength coverage.

In the subsections below we describe how these derived quantities change as a function of the number of stars. The following figures also represent the distribution of expected values, indicating the 1/99 and 10/90 percentiles. Contrary to the standard way of delivering evolutionary model predictions, FASTAR allows the user to synthesize any arbitrary number of models. Thus, these percentiles boundaries are not designed to formally describe the behavior of the line strengths, colors etc. but to exemplify the range of possible values. Note also that the variation in these quantities should not be interpreted as a model uncertainty but as a consequence of the intrinsic stochasticity of semi-resolved evolutionary stellar population models.

4.1. Line-strengths indices

Figure 2 shows the behavior of the H_{β_o} (Cervantes & Vazdekis 2009, top panel), the Mgb (Worthey et al. 1994, middle panel), and the TiO_2 (Faber et al. 1985; Trager et al. 1998, bottom panel) line-strength indices as a function of the number of stars for a 10 Gyr old population with solar metallicity, and Milky Way-like IMF. These three indices are mostly sensitive to age, metallicity and IMF slope, respectively, and exemplify how line-strength predictions can vary in the semi-resolved regime even when the underlying population has the same physical properties. Shaded blue areas indicate the 1/99 and 10/90 distribution percentiles over 1,000,000 realizations, while the solid blue line shows the median value. We increase the number of realizations when decreasing the number of stars to capture the enhanced variability of the model predictions. For comparison, each panel also includes dashed horizontal lines corresponding to the line-strength values expected when changing the stellar population properties for a fully sampled SSP model.

When the number of stars falls below $N_{\text{stars}} \sim 10^5$ per resolution element, the stochastic fluctuations of the models become the dominant factor, inducing changes in the observed line-strength indices much larger than those expected from variations in age, metallicity, or the IMF (dashed horizontal lines). The asymmetric distribution around the median value results from the sampling of specific stellar masses and thus evolu-

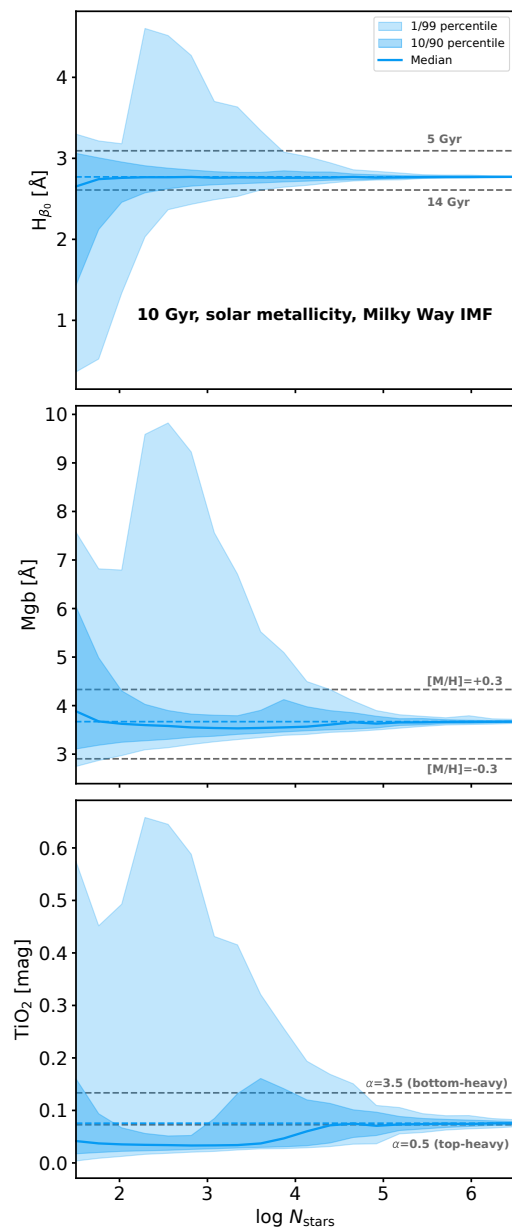


Fig. 2: Behavior of line-strength indices. From top to bottom, the distribution of FASTAR semi-resolved predictions as a function of the number of stars in the population is shown for the H_{β_o} , Mgb, and TiO_2 features, respectively. These distributions correspond to 1,000,000 stochastic IMF samplings of the same 10 Gyr old, solar metallicity, and Milky Way-like IMF population. The median of the distribution is shown with a solid blue line and the shaded regions correspond to the 10/90 and 1/99 percentiles. The blue dashed line indicates the fully sampled SSP FASTAR prediction. For comparison, dashed horizontal lines mark the line-strength value expected in the fully sampled regime for various ages, metallicities and IMFs. Line-strength values have been calculated at the nominal 2.51 \AA resolution of the FASTAR models.

tionary phases (e.g. low-mass main sequence, turn-off, or giant star) when changing the number of stars in the population. This is clearly exemplified by the TiO_2 behavior. This index is more prominent in the atmospheres of cool giant stars (e.g., Spiniello et al. 2014), and therefore the measured line strengths are biased towards low TiO_2 values if the number of stars is

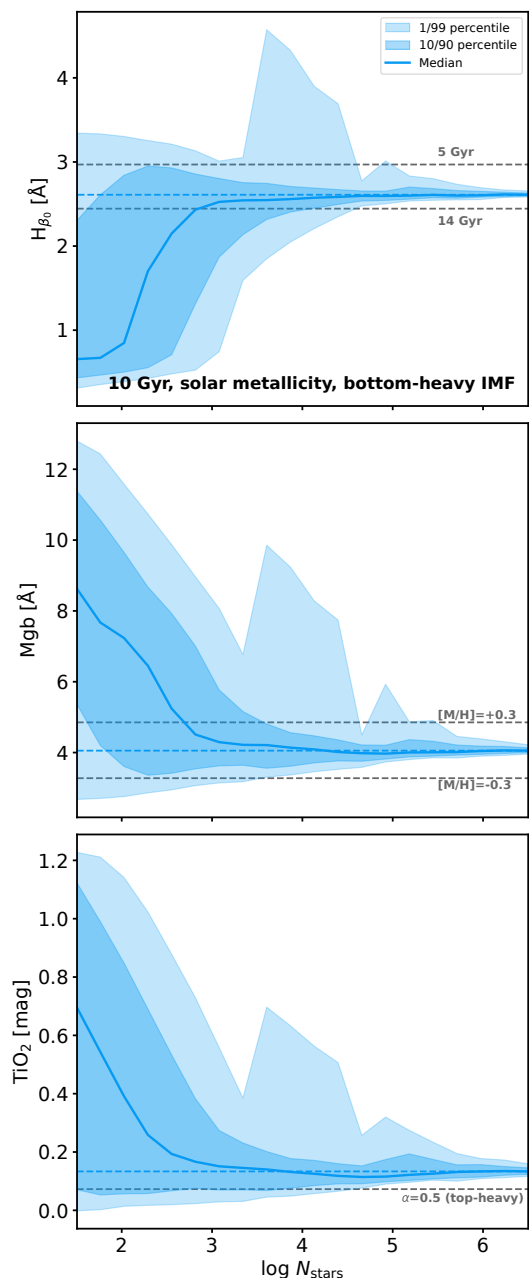


Fig. 3: Same as Fig. 2 but line-strength predictions have been calculated assuming a single power law, bottom-heavy IMF ($\alpha = 3.5$).

low. Only when the contribution of the more massive and less frequent giant stars rises through a larger number of stars, the distribution of TiO_2 values converges towards the fully sampled SSP expectation. Interestingly, neither H_{β_0} nor Mgb exhibit clear biases as the number of stars decreases. In general, if the number of stars is low, line-strength measurements cannot be directly translated to physical parameters. For completeness, appendix A includes a similar assessment but for a young (0.25 Gyr) population.

It is evident from Fig. 2 that, in the semi-resolved regime, the recovered spectral properties are a balance between the intrinsic properties of the stellar population and the IMF and stellar evolution sampling, which depends on the number of stars per resolution element. Therefore, in this regime, the choice of

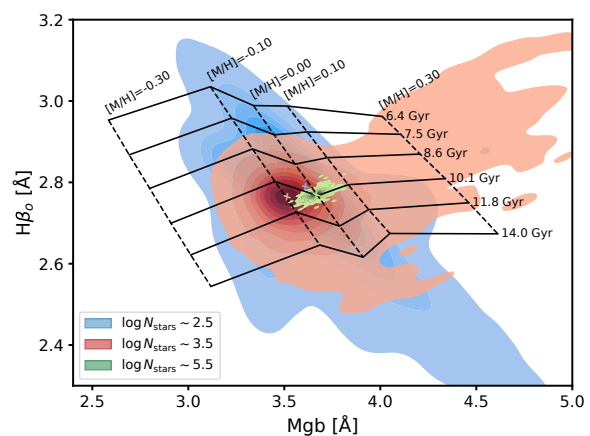


Fig. 4: Semi-resolved index–index diagrams. Black lines correspond to the fully sampled H_{β_0} – Mgb FASTAR predictions for different ages and metallicities, as noted by the labels. On top, green, red, and blue contours show FASTAR index–index distributions for $N_{\text{stars}} = 10^{5.5}$, $10^{3.5}$, and $10^{2.5}$, respectively, for a population with solar metallicity and an age of 10 Gyr. Colored marks indicate the median of the distributions.

the IMF has a strong effect on the model predictions. Figure 3 is equivalent to Fig. 2 but in this case, the FASTAR semi-resolved predictions have been calculated assuming a single power law, bottom-heavy IMF (unimodal, $\alpha = 3.5$). While there are obvious similarities between both figures, it is also clear that the IMF has an important role in modulating the behavior of the three indices. In particular, Fig. 3 does show clear biases in the measured line-strength values when decreasing the number of stars, with weaker H_{β_0} values and stronger Mgb and TiO_2 features as the number of stars decreases.

The intrinsic spread in semi-resolved spectral predictions, and consequently in the derived line-strength indices, places clear limits on how accurately stellar population parameters can be constrained from individual line-strength measurements². This effect is further illustrated in the H_{β_0} – Mgb grid shown in Fig. 4. Such index–index diagrams are commonly used in detailed spectroscopic analyses (e.g., Worthey et al. 1992; Thomas et al. 2005; Kuntschner et al. 2010; La Barbera et al. 2019) since, in the fully sampled regime, a pair of line-strength measurements can (in principle) fully determine the properties of the underlying stellar population. These unique predictions for standard fully sampled SSP models are shown as a black grid in Fig. 4.

In the semi-resolved regime, however, the prospects are different. The green, red, and blue contours in Fig. 4 show the projected distributions of line-strength measurements (from Fig. 2) for $\log N_{\text{stars}} = 5.5$, 3.5 , and 2.5 , respectively. Even for a relatively large number of stars (green contours) the stochastic nature of finite, semi-resolved populations can introduce a scatter up to ~ 0.1 dex in metallicity and ~ 1 Gyr in age, despite all measurements corresponding to the same 10 Gyr, solar-metallicity model. For smaller numbers of stars per resolution element (red and blue contours), the scatter becomes much larger, with line-strength values extending well beyond the boundaries of the

² Note, however, that the shaded areas in Figs. 2 and 3 represent the expected range of model values and should not be interpreted as uncertainties in the recovered stellar population parameters. The latter will depend on the specific fitting approach and on the properties of the data.

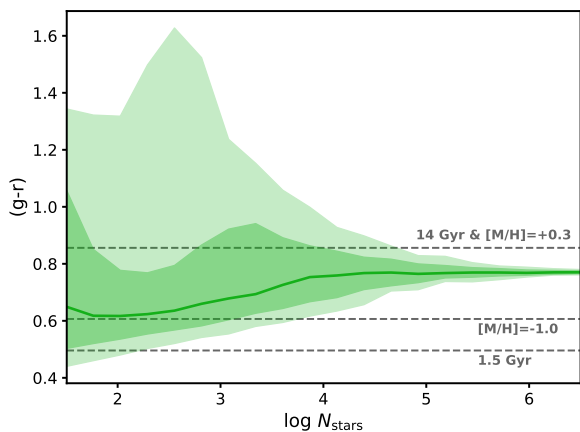


Fig. 5: Color dependence on the number of stars. Green shaded areas indicate the 10/90 and 1/99 percentiles of the distribution of measured $(g-r)$ colors as a function of N_{stars} for semi-resolved populations of 10 Gyr, solar metallicity and a Milky Way-like IMF. The green solid line corresponds to the median trend. For reference, horizontal dashed lines mark the FASTAR color prediction for a fully sampled IMF with different ages and metallicities.

original model grid. In addition, small systematic biases emerge as the number of stars decreases.

4.2. Colors

Colors of semi-resolved populations can also be computed directly with FASTAR by convolving the model spectra with any desired set of photometric filters. As noted above, FASTAR models can be generated with full spectroscopic detail over the 3,540–7,400 Å wavelength range, and for photometric applications over a broader 2,000–12,000 Å coverage. To illustrate the impact of stochastic IMF sampling in semi-resolved populations, Fig. 5 shows the predicted $(g-r)$ color, as in Fig. 2, calculated for a 10 Gyr, solar-metallicity population with a Milky Way-like IMF, using the narrower FASTAR wavelength range.

The impact of stochasticity on the integrated colors of semi-resolved populations is larger than that observed in the line-strength indices. Even when the population is composed of $\sim 10^5$ stars, the 16/84 percentile variation ($\sim \pm 1\sigma$) in the measured $(g-r)$ color is ~ 0.09 mag. When N_{stars} is even lower, the range of possible colors increases, becoming compatible, under the assumption of a fully sampled IMF, with a range of ages and metallicities, as indicated by the horizontal dashed lines in Fig. 5. On top of this large color scatter, a bias towards blue $(g-r)$ colors is also evident as the number of stars in the population decreases (e.g., Cerviño & Valls-Gabaud 2003), reaching a minimum around $\log N_{\text{stars}} \sim 2$.

A large scatter in the color predictions for a given stellar population casts further doubts on the validity of standard analysis approaches when dealing with semi-resolved stellar systems. Figure 6 shows, in black, the fully sampled FASTAR predictions for the $(g-r)$ vs Mgb plane and in colored contours (green, red, and blue) semi-resolved realizations with $\log N_{\text{stars}} = 5.5, 3.5,$ and 2.5, respectively. The range of ages and metallicities of the grid is the same as in Fig. 4.

The increased scatter combined with the lesser sensitivity to changes in the stellar population properties of colors vs line-

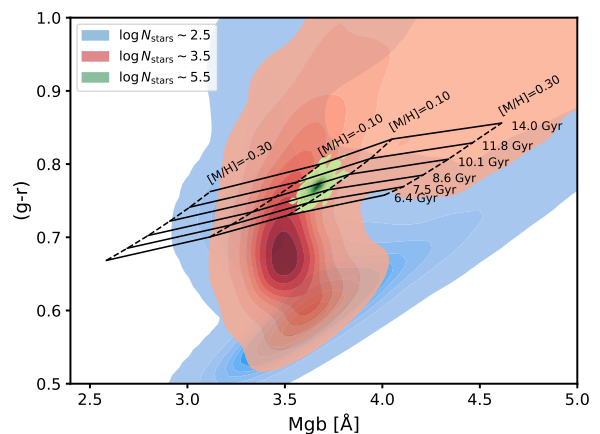


Fig. 6: Color grid. Black lines indicate the FASTAR fully sampled predictions for the same age and metallicity ranges as in Fig. 4. Green, red, and blue contours show the distributions of $(g-r)$ and Mgb values for a 10 Gyr and solar metallicity population with a variable number of stars ($N_{\text{stars}} = 10^{5.5}, 10^{3.5},$ and $10^{2.5}$, respectively).

strengths is evident from Fig. 6. With populations as well sampled as $N_{\text{stars}} \sim 10^5$, the range of possible ages covers from ~ 6 to ~ 14 Gyr. When the number of stars drops below that threshold, the $(g-r)$ –Mgb loses almost all predictive power, with a large spread of possible solutions and a clear bias towards blue colors.

4.3. Mass-to-light ratios

In conjunction with the properties of the stellar population (age, metallicity and IMF in the case of the FASTAR models), the number of stars is the fundamental parameter determining the resulting spectra of semi-resolved populations. In the fully sampled regime, the number of stars and the observed mass-to-light ratio are rigidly tied through the assumed IMF. Therefore, when the IMF is fully sampled, the observed luminosity of a stellar population can be directly translated into a stellar mass, or equivalently into a number of stars, through the expected mass-to-light ratio.

However, in semi-resolved populations, the mapping between mass, luminosity, and number of stars breaks apart because of the stochastic sampling of the IMF. Illustrating how the mass-to-light ratio of a given population varies in the semi-resolved regime, Fig. 7 shows the predicted r -band mass-to-light ratio as a function of N_{stars} , assuming again a 10 Gyr, solar metallicity and Milky Way-like IMF. As before, shaded areas denote the 10/90 and 1/99 percentiles of the distribution and the solid line indicates the median relation.

As in the previous figures, the intrinsic variability in the IMF sampling results in a wide range of actual mass-to-light ratios. While there is a clear bias towards high values as N_{stars} decreases, and therefore low-mass stars become more prominent with respect to higher and brighter stellar masses, the scatter can expand more than an order of magnitude, which is consistent with the expectations of both a very old and a very young population (horizontal dashed lines in Fig. 7).

Figure 7 showcases the difficulty of measuring the stellar mass of a semi-resolved stellar population based on its stellar population properties. Alternatively, mass-to-light ra-

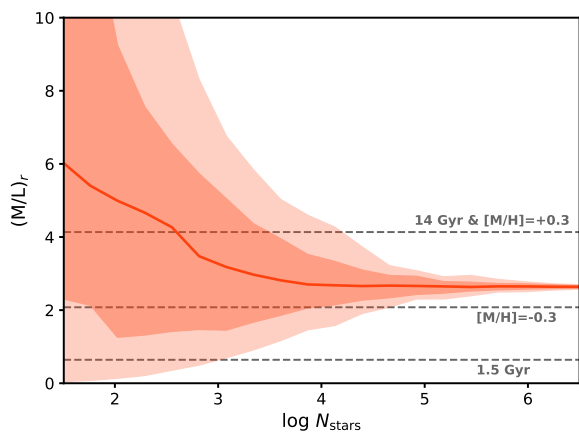


Fig. 7: Mass-to-light ratio. The measured r -band mass-to-light ratio for a 10 Gyr and solar metallicity population is shown as a function of the number of stars in the semi-resolved FASTAR models. Shaded areas correspond to the 10/90 and 1/99 percentiles of the distribution of retrieved values after the stochastic sampling of the IMF. The solid red line indicates the median value for each N_{stars} bin.

tios can also be estimated on the basis of scaling relations (e.g., Bell & de Jong 2001; Bell et al. 2003; Zibetti et al. 2009; McGaugh & Schombert 2014). In practice, this is done by plugging in observed colors into equations calibrated using standard SSP models to retrieve an approximate mass-to-light in a given photometric band.

Following this approach, Fig. 8 compares the r -band mass-to-light ratios estimated from the $(g-r)$ calibration of Roediger & Courteau (2015) with the intrinsic values measured from the FASTAR semi-resolved predictions. As before, we show the ratio between the predicted and intrinsic mass-to-light values as a function of the number of stars. The logarithmic scale on the vertical axis therefore represents the systematic error that would be incurred when using color vs mass-to-light calibrations derived from fully integrated models to estimate the stellar mass of semi-resolved populations. It is clear that color-based estimates of the mass-to-light ratio can lead to significant discrepancies between the predicted and true stellar masses of semi-resolved populations, with differences of up to ~ 1 dex in the recovered stellar mass when the number of stars falls below $\sim 10^4$, which has evident implications in, for example, measured scaling relations. Yet, the fact that empirical calibrations retain some information in the semi-resolved regime is likely due to the fact that they are ultimately sensitive to the color-luminosity-mass relation of individual stars, which are the base of both semi-resolved and fully sampled SSP models. Both Figs. 7 and 8 highlight a fundamental limitation inherent to the semi-resolved regime: the number of stars is a critical parameter in determining the properties of the emitted flux, yet, its determination poses a nontrivial observational challenge.

5. Semi-resolved observations

FASTAR offers the possibility of modeling the complexity of semi-resolved stellar populations within the same framework as standard evolutionary synthesis models assuming a fully sampled IMF. As noted above, however, it is not trivial to observationally determine whether all the evolutionary phases across the IMF are sufficiently well samples in a given observation. Cur-

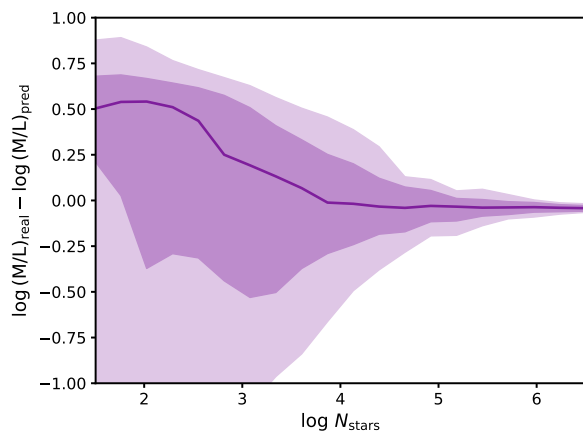


Fig. 8: Color-based mass-to-light ratio estimates. The (logarithmic) ratio between the intrinsic mass-to-light ratio and that estimated using the color relations of Roediger & Courteau (2015), computed as a function of N_{stars} for a 10 Gyr and solar metallicity FASTAR semi-resolved population. As in the figures above, shaded areas correspond to the 10/90 and 1/99 percentiles of the measured distribution while the solid purple line corresponds to the median.

rently, the study of the low-surface brightness is Universe, arguably, one of the most evident situations where the stochastic sampling of the IMF might have relevant impact.

In Fig. 9 we make use of the unique features of FASTAR to predict the effect of stochastic observations at different r -band surface brightness levels. Specifically, we show a series of arbitrary realizations of the $(g-r)$ color of a semi-resolved old and metal-poor population (10 Gyr, $[M/H] = -1.5$, as expected for the outskirts of a massive galaxy or in an extended low-mass object) vary with surface brightness. This surface brightness was calculated using the measured r -band absolute magnitude of each model realization, assuming that the population is at a typical distance of 15 Mpc (i.e. that of the Virgo cluster) and that the resolution element is 1 arcsec² (i.e. average seeing).

At this distance and according to Fig. 9, the $\log N_{\text{stars}} \sim 10^5$ threshold where the stochasticity of semi-resolved populations starts to dominate occurs at $\mu_r \sim 25$ mag arcsec⁻², well within our current technical capabilities (e.g., Golini et al. 2024; Khim et al. 2025; Li et al. 2025; Euclid Collaboration et al. 2026). For $\mu_r \sim 28$ there is a sudden increase in the predicted $(g-r)$ values, interpreted as the stochastic fluctuations introduced by the appearance of (red) giant stars. This is a natural prediction of semi-resolved models and should be observable even with the color uncertainty expected at this low-surface brightness level. Evidently, the exact location of this peak depends on the distance to the object and on the physical scale of the resolution element of the observations. Towards fainter magnitudes, there is an evident bias towards blue $(g-r)$ as already shown in Fig. 5.

It is worth emphasizing that the correlation between scatter, observed colors, and brightness maps results from the prevalence of different stellar evolutionary phases along the isochrone as N_{stars} changes. To further illustrate this relation between isochrones (and thus stellar evolution theory) and colors, Fig. 10 shows, for two different N_{stars} , how the predicted colors scale with the surface brightness level of the population. As in the figure above, color predictions in Fig. 10 correspond to a 10 Gyr old and $[M/H] = -1.5$ stellar population.

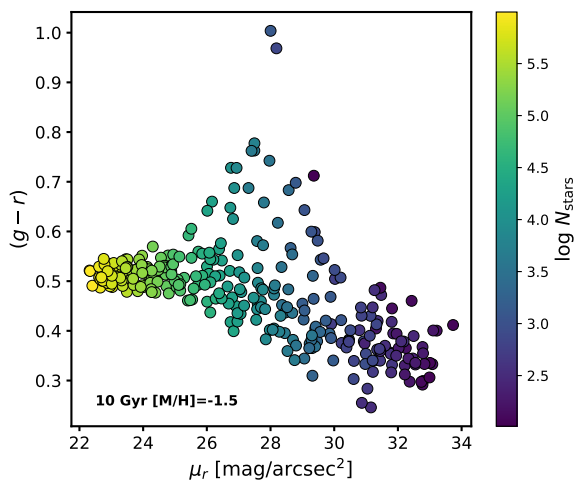


Fig. 9: Colors at the Virgo distance. Colored symbols represent 300 $(g - r)$ FASTAR semi-resolved predictions for an old (10 Gyr) and metal-poor population, observed at a distance of 15 Mpc through a 1 arcsec² resolution element, representing the typical properties expected at low surface brightnesses in relatively nearby galaxies. These random FASTAR $(g - r)$ realizations are shown with varying number of stars (from left to right, as indicated by the color bar), as a function of the predicted r -band surface brightness.

The top panel of Fig. 10 is particularly revealing. For $N_{\text{stars}} = 100$, the color-surface brightness plane reproduces the shape of the underlying isochrone and most of its evolutionary features. As the number of stars increases, $N_{\text{stars}} = 100,000$ in the bottom panel of Fig. 10, the variability decreases and becomes entirely dominated by fluctuations in the distribution of giant stars. Vertical dashed lines in the top panel indicate the color range probed by the bottom one, demonstrating that, in the latter, fluctuations are driven by the stochastic sampling of giant stars. In this line, redder colors than the $(g-r)$ shown here tend to be more sensitive to the brighter (and cooler) giant population, while fluctuations in bluer colors probe hotter evolutionary phases. Note also how, in practice, Fig. 10 corresponds approximately (given that $N_{\text{stars}} \propto \mu_r$) to a vertical slice of the scatter in Fig. 9.

While Fig. 9 illustrates the importance that semi-resolved stellar populations already have in the analysis of low-surface brightness features, the upcoming generation of 40-meter-class telescopes possess a much greater challenge for fully sampled evolutionary stellar population models. With milli-arcsecond projected scales, the stochastic nature of semi-resolved populations will be noticeable at much higher surface brightnesses. Figure 11 represents, the $(g - r)$ color of an average old (10 Gyr) and solar metallicity population observed at 100 Mpc (i.e. the Coma cluster) through a 5 milli-arcsecond scale instrument.

Interpreting the $(g - r)$ trend and scatter in terms of the relation between IMF and stellar evolution sampling is rather evident from Fig. 11. For very low N_{stars} the synthesized FASTAR model is dominated by the red colors of very low-mass stars³. Then, with increasing N_{stars} , the color becomes bluer as the main sequence turn-off becomes more heavily sampled, reaching a minimum at around $\mu_r \sim 25$ mag arcsec⁻². The emergence of giant stars clearly appears, in this case, at $\mu_r \sim 19$ mag arcsec⁻².

³ In this very low N_{stars} regime, however, the use of evolutionary stellar population models may not be the most convenient approach.

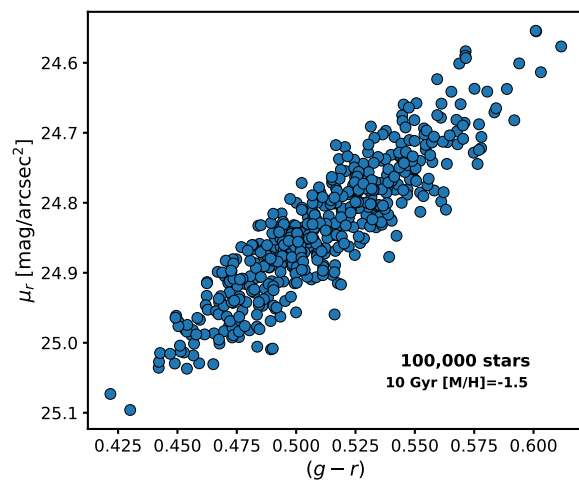
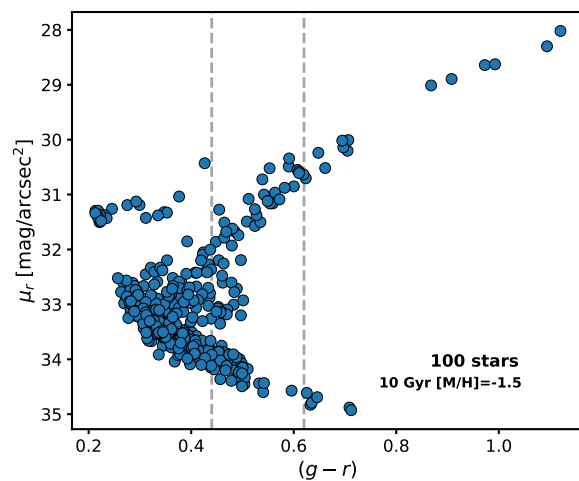


Fig. 10: Isochrone mapping. Both panels represent the predicted $(g - r)$ color and μ_r surface brightness for the same old and metal-poor population of Fig. 9, observed as well with a 1 arcsec pixel scale at 15 Mpc. Each point is a different FASTAR realization with the same age, metallicity, IMF and number of stars. In the top panel, FASTAR predictions are shown for a semi-resolved population of 100 stars. Because of the sparse sampling of the IMF and thus of the different stellar evolutionary phases, the color and brightness fluctuations effectively map the underlying isochrone used to construct the model. In the bottom panel, FASTAR predictions are shown for the cases of having 100,000 stars. Measured surface brightnesses are therefore higher than in the upper panel, but exhibiting milder variations driven by red giant stars. Dashed vertical lines in the top panel illustrate the color range probed in the bottom one.

Once all stellar masses and thus evolutionary phases average out, the FASTAR $(g - r)$ converges towards the expected value of a fully sampled SSP model of 10 Gyr and solar metallicity. For a formal characterization of these biases we refer the reader to [Cerviño & Valls-Gabaud \(2003\)](#).

The most striking difference between Fig. 9 and Fig. 11 is the surface brightness level at which stochasticity emerges. In a nearby galaxy observed with a typical seeing (Fig. 9), semi-resolved modeling becomes necessary for $\mu_r \gtrsim 25$ mag arcsec⁻². However, even at 100 Mpc, a galaxy observed with milli-arcsecond resolution (Fig. 11) will show signs of stochasticity in the observed data at surface brightnesses as high as $\mu_r \sim$

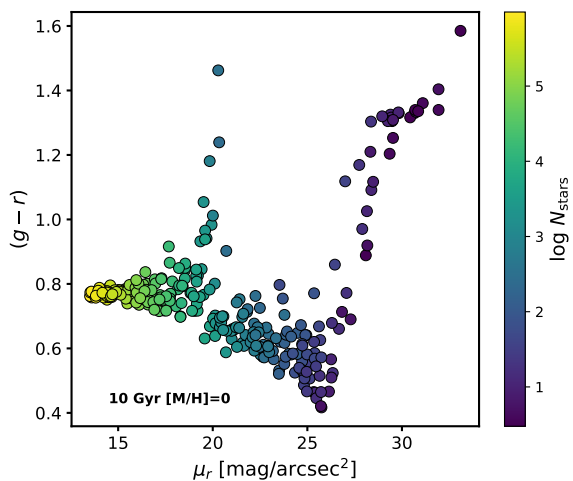


Fig. 11: Predictions for 40-meter-class telescopes. Semi-resolved $(g-r)$ color predictions as a function of μ_r for an old (10 Gyr) and solar metallicity population at a distance of 100 Mpc observed projected into a 5 milli-arcsec per pixel scale, emulating a typical stellar population as observed through a 40-meter-class telescope. The effect of the stochastic sampling of the IMF becomes evident at surface brightnesses as high as $\mu_r \sim 19$ mag arcsec $^{-2}$. Symbols are color-coded according to the number of stars in the semi-resolved FASTAR stellar population model.

19 mag arcsec $^{-2}$. For reference, only the innermost few arcseconds of the most massive galaxies in the Coma cluster reach high enough surface brightnesses (e.g., Strom & Strom 1978) to be analyzed with fully sampled SSP models. In practice, in the era of 40-meter telescopes, Fig. 11 demonstrates that precise stellar population analyses in the local Universe will inevitably require the implementation of semi-resolved models.

6. Stochastic predictions: Blessing or curse

In the sections above we have shown how FASTAR semi-resolved predictions are stochastic by nature. This is a fundamental difference with respect to standard evolutionary stellar population model predictions where the integral synthesis described by Eq. 1 uniquely define the model output. This synthesis uniqueness is what justifies the use of SSP models and derived quantities such as line-strengths indices and colors to translate the spectro-photometric properties of galaxies into physically meaningful quantities.

The scatter in the semi-resolved predictions is not meaningless as it probes the biased sampling of specific stellar evolutionary phases and therefore encodes valuable information about the underlying stellar population content. In fact, fully sampled SSP models can be also understood as the mean value expected from a finite distribution of stars (e.g., Cerviño & Luridiana 2006) whose scatter tends to zero as the number of stars increases. Therefore, beyond the mean, higher orders of these distributions can be computed as additional constraints on the stellar population content of galaxies (e.g., Vazdekis et al. 2020), this being the central idea behind the scientific exploitation of surface brightness fluctuations (e.g., Tonry & Schneider 1988; Blakeslee et al. 2009; Rodríguez-Beltrán et al. 2021). Furthermore, Figs. 9, 10, and 11 demonstrate how a set of independent measurements can be used as direct tests on the isochrones physics. This is a unique advantage of semi-resolved stellar pop-

ulations, as they enable calibrating our knowledge on stellar evolution beyond the limited environment of the Milky Way.

Dealing with semi-resolved observations requires at the same time dedicated analysis strategies. Figures 4 and 6 show-case how standard observables such as colors and line-strength indices can present strong deviations compared to fully sampled SSP predictions (e.g., Cerviño et al. 2008). This at first sight may appear counterintuitive since averaging a large number of measurements does not lead to the average SSP value, but is simply due to the fact that equivalent widths, magnitudes, colors, mass-to-light ratios etc. are all nonlinear operations over the emitted spectra.

It is important to emphasize that FASTAR predictions are designed to model actual observations. The proposed random sampling of the IMF emulates, for example, the situation in which independent regions of the same globular cluster are observed in a semi-resolved manner. Even if all stars in the globular cluster share the same age and chemical composition and follow the same underlying IMF, observations of different regions will correspond to independent realizations of the IMF with a finite number of stars. However, because these realizations are drawn from a common IMF, combining multiple independent regions into a single measurement naturally converges toward the fully sampled IMF limit, i.e., the integral predictions of standard SSP models. Semi-resolved FASTAR predictions therefore constitute a natural extension of traditional evolutionary stellar population models and can be used in a similar way to fit the spectro-photometric properties of external galaxies.

Does this have real-world implications? Currently, the most evident scientific case where semi-resolved populations are at play is in the analysis of low-surface brightness features. In this regime, any stellar population signal is typically below the observational noise in the data and therefore averages (e.g. over elliptical apertures) become mandatory. However, the way in which averages are computed can have important consequences. For example, calculating an average $(g-r)$ color as the mean of the all the individual $(g-r)$ colors of every pixel will lead to the biases show in Figs. 4 and 6, with the subsequent advantages and disadvantages. On the contrary, an average color measured by first averaging counts in the g and r bands and then calculating their magnitude difference will result, if the number of pixels is sufficiently large, into a fully sampled, SSP-equivalent measurement (assuming a linear behavior of the detector and data reduction).

The analysis of low-surface-brightness populations presents additional challenges. Specifically, in relatively shallow observations, different evolutionary phases are expected to exhibit different signal-to-noise ratios. In particular, low-mass stars will typically contribute to the integrated properties with noisier spectra than more luminous giants. This systematic dependence of the signal-to-noise ratio on stellar luminosity may introduce additional biases beyond those discussed in the sections above, where noise was not considered. This a potential issue affecting of both semi-resolved and standard SSP models. The formalism behind the synthesis of FASTAR predictions allows for a consistent treatment of this effect. In particular, individual stellar spectra can be combined while explicitly accounting for different noise levels. Although this feature is not implemented by default, the open-source nature of FASTAR makes it straightforward to incorporate.

While the joint analysis of a large number of independent measurements offers a viable way forward to extract information from semi-resolved observations, being able to analyze individual spectro-photometric measurements remains, for obvi-

ous reasons, a desirable goal. The stochastic nature of semi-resolved observations poses, however, an evident challenge. Standard inversion algorithms cannot deal with the inherent variability of semi-resolved models, as the same input parameters (age, metallicity, IMF and number of stars in the case of FASTAR) can result in drastically different model outputs. In this context, simulation based inference approaches offer a clear and formal way forward to deal with such intractable likelihoods (e.g., [Hahn & Melchior 2022](#); [Angeloudi et al. 2023, 2024, 2025](#); [Iglesias-Navarro et al. 2024, 2025](#)) and the efficient synthesis of semi-resolved FASTAR models is particularly well-suited for these forward modeling tasks, as we will exemplify in upcoming papers. Complementary, FASTAR also offers the framework to combine independent measurements of the same stellar population in order to derive tighter observational constraints.

This interpretation of semi-resolved observations must also consider the possibility of composite stellar populations. It can be argued that as the physical scale probed within a galaxy decreases, and consequently N_{stars} decreases, the stellar population properties become progressively simpler. For example, the integrated spectrum of a spiral galaxy containing both a bulge and a disc is generally more complex than the spectra of each component separately. Observations at smaller spatial scales therefore tend to minimize the effect of radial stellar population gradients, justifying the SSP assumption. Nevertheless, as in standard SSP models, the spectrum of a composite population remains a linear combination of the spectra of the individual subpopulations. Semi-resolved models therefore preserve the linearity that underlies most population inference techniques, allowing composite populations to be incorporated naturally within inversion frameworks in much the same way as in fitting methods based on fully sampled SSP models (e.g., [Cappellari & Emsellem 2004](#); [Ocvirk et al. 2006](#); [Carnall et al. 2018](#); [Johnson et al. 2021](#)). In practice, this means that semi-resolved modeling does not introduce a fundamentally different treatment of composite populations, but rather extends the standard SSP framework to regimes where IMF sampling becomes relevant.

Finally, a note on the term semi-resolved. Throughout this paper, we use this term to describe situations in which the number of stars per resolution element is not large enough to properly sample all stellar evolutionary phases along an isochrone, and therefore constitutes a regime in which the standard integral synthesis of evolutionary stellar population models (Eq. 1) does not strictly apply. Because different stellar evolutionary phases present prominent color differences, the boundary between both regimes depends on the exact wavelength range (e.g., [Cerviño & Luridiana 2004](#)). As clearly explained in Section 1 of [Conroy & van Dokkum \(2016\)](#), the concept of a semi-resolved population is intended to capture the intermediate regime between observations in which all individual stars can be resolved and the opposite extreme, in which the observed spectra are effectively composed of an infinite number of stars. In many semi-resolved situations, however, one should not expect individual stars to be partially resolved, as observations will only capture their integrated flux. In short, semi-resolved evolutionary stellar population models aim to reproduce the combined flux of a relatively small number of stars with the same age and chemical composition, all observed within a single resolution element.

7. Summary

FASTAR enables the modeling of semi-resolved stellar populations based on the same evolutionary principles as standard SSP

models. Thanks to its computational efficiency, semi-resolved models can be computed on the fly over a wide range of ages and metallicities. The combination of empirical and theoretical stellar libraries allows for detailed spectroscopic predictions from 3,540 to 7,400 Å and from 2,000 to 12,000 Å for photometric applications. The calibration of the FASTAR models ensures that arbitrary line-strength indices, colors, magnitudes, and mass-to-light ratios can be computed.

Beyond the description of the model synthesis, the main features of FASTAR semi-resolved predictions are as follows:

- Semi-resolved predictions share the same assumptions of standard evolutionary stellar population models but naturally extend their applicability range from fully-integrated to fully-resolved observations.
- Stochastic variations in the model predictions are noticeable even if the number of stars is as high as $N_{\text{stars}} \sim 10^6$. When the number of stars drops below $N_{\text{stars}} \sim 10^{4.5}$, stochasticity becomes a dominant factor determining the properties of FASTAR semi-resolved spectra.
- Line-strength indices traditionally used to infer stellar population properties from integrated spectra lose much of their constraining power in the semi-resolved regime. For broader photometric measurements such as colors, the effect of stochasticity is even more pronounced. The scatter and potential biases in the line-strengths and colors of semi-resolved populations heavily depend on the adopted IMF.
- While the number of stars is a critical parameter in modeling semi-resolved populations, it is challenging to constrain from observations as the mass-to-light ratio in the semi-resolved regime can present large variations and systematic biases even if the underlying stellar population parameters (namely age, metallicity and IMF) remain constant. Mass-to-light ratio approximations based on color scaling relations present similar difficulties.
- The behavior of semi-resolved FASTAR spectra as a function of N_{stars} is driven by the incomplete sampling of different stellar evolutionary phases. Only when all these phases are properly sampled, FASTAR predictions converge towards the integral formulation. Conversely, semi-resolved observations can be used as direct tests of stellar evolution theory.
- FASTAR models predict that stochastic effects should be already noticeable in low-surface brightness studies. Looking ahead, semi-resolved observations are expected to be the norm for the next generation of 40-meter telescopes.

Semi-resolved stellar populations pose important technical challenges. The inherent stochasticity due to the incomplete IMF sampling implies that there are no unique predictions, rendering standard stellar population inversion algorithms unusable. Furthermore, at a deeper level, stellar atmospheres do not contain information about the age or (evidently) IMF of a population. Therefore, from the point of view of the integrated light, these quantities are only measurable when analyzing a sufficiently large collection of coeval stars. Thus, contrary to standard fully sampled evolutionary models, in the semi-resolved regime our ability to determine ages and IMFs is inevitably conditioned by the total number of stars in our resolution element.

While the distribution of observed values (brightnesses, colors, line indices etc.) holds value information about the properties of semi-resolved populations, analysis approaches able to fit individual observations are highly desirable in order to maximize the information extracted from current and upcoming facilities. In this context, FASTAR used in combination with new

techniques such as simulation-based inference frameworks (e.g., Hahn & Melchior 2022; Iglesias-Navarro et al. 2024, 2025) offers a promising way forward.

Acknowledgements. We would like to thank the referee for the insightful and constructive interactions. We acknowledge support from grant PID2022-140869NB-I00 funded by the Spanish Ministry of Science and Innovation, from PID2022-136598NB-C33 funded by MCIN/AEI/10.13039/501100011033 and by “ERDF A way of making Europe”. F.L.B. acknowledges support from INAF minigrant 1.05.23.04.01. We would like to thank Ignacio Ferreras and Ignacio Trujillo for their insightful comments during the development of FASTAR.

Models availability

Documentation and examples on how to use FASTAR can be found at the project’s website <https://fastar.readthedocs.io>

The code is freely available here <https://github.com/inavarro/fastar>

References

- Abraham, R. G. & van Dokkum, P. G. 2014, *PASP*, 126, 55
- Alsing, J., Peiris, H., Leja, J., et al. 2020, *ApJS*, 249, 5
- Angeloudi, E., Falcón-Barroso, J., Huertas-Company, M., et al. 2024, Constraints on the in situ and ex situ stellar masses in nearby galaxies obtained with artificial intelligence
- Angeloudi, E., Falcón-Barroso, J., Huertas-Company, M., et al. 2023, *MNRAS*, 523, 5408
- Angeloudi, E., Huertas-Company, M., Falcón-Barroso, J., et al. 2025, *A&A*, 703, A290
- Beerman, L. C., Johnson, L. C., Fouesneau, M., et al. 2012, *ApJ*, 760, 104
- Bell, E. F. & de Jong, R. S. 2001, *ApJ*, 550, 212
- Bell, E. F., McIntosh, D. H., Katz, N., & Weinberg, M. D. 2003, *ApJS*, 149, 289
- Bica, E. 1988, *A&A*, 195, 76
- Bica, E. & Alloin, D. 1986, *A&A*, 162, 21
- Bittner, A., Sánchez-Blázquez, P., Gadotti, D. A., et al. 2020, *A&A*, 643, A65
- Blakeslee, J. P., Jordán, A., Mei, S., et al. 2009, *ApJ*, 694, 556
- Bradbury, J., Frostig, R., Hawkins, P., et al. 2018, JAX: composable transformations of Python+NumPy programs
- Branco, V., Coelho, P. R. T., Lançon, A., Martins, L. P., & Prugniel, P. 2024, *A&A*, 687, A142
- Bruzual, G. & Charlot, S. 2003, *MNRAS*, 344, 1000
- Bruzual A., G. 2002, in *IAU Symposium*, Vol. 207, Extragalactic Star Clusters, ed. D. P. Geisler, E. K. Grebel, & D. Minniti, 616
- Buzzoni, A. 1993, *A&A*, 275, 433
- Cappellari, M. & Emsellem, E. 2004, *PASP*, 116, 138
- Carnall, A. C., McLure, R. J., Dunlop, J. S., & Davé, R. 2018, *MNRAS*, 480, 4379
- Cervantes, J. L. & Vazdekis, A. 2009, *MNRAS*, 392, 691
- Cerviño, M. 2013, *New A Rev.*, 57, 123
- Cerviño, M. & Luridiana, V. 2004, *A&A*, 413, 145
- Cerviño, M. & Luridiana, V. 2006, *A&A*, 451, 475
- Cerviño, M., Luridiana, V., & Castander, F. J. 2000, *A&A*, 360, L5
- Cerviño, M., Luridiana, V., & Jamet, L. 2008, *A&A*, 491, 693
- Cerviño, M. & Valls-Gabaud, D. 2003, *MNRAS*, 338, 481
- Cerviño, M., Valls-Gabaud, D., Luridiana, V., & Mas-Hesse, J. M. 2002, *A&A*, 381, 51
- Chabrier, G. 2003, *PASP*, 115, 763
- Conroy, C. 2013, *ARA&A*, 51, 393
- Conroy, C. & van Dokkum, P. G. 2012, *ApJ*, 760, 71
- Conroy, C. & van Dokkum, P. G. 2016, *ApJ*, 827, 9
- da Silva, R. L., Fumagalli, M., & Krumholz, M. 2012, *ApJ*, 745, 145
- De Marchi, G., Paresce, F., & Portegies Zwart, S. 2005, in *Astrophysics and Space Science Library*, Vol. 327, The Initial Mass Function 50 Years Later, ed. E. Corbelli, F. Palla, & H. Zinnecker, 77
- Dey, A., Schlegel, D. J., Lang, D., et al. 2019, *AJ*, 157, 168
- Drory, N., Blanc, G. A., Kreckel, K., et al. 2024, *AJ*, 168, 198
- Eldridge, J. J. 2012, *MNRAS*, 422, 794
- Euclid Collaboration, Mellier, Y., Abdurro’uf, et al. 2025, *A&A*, 697, A1
- Euclid Collaboration, Urbano, M., Duc, P.-A., et al. 2026, *A&A*, 707, A229
- Faber, S. M. 1972, *A&A*, 20, 361
- Faber, S. M., Friel, E. D., Burstein, D., & Gaskell, C. M. 1985, *ApJS*, 57, 711
- Falcón-Barroso, J., Sánchez-Blázquez, P., Vazdekis, A., et al. 2011, *A&A*, 532, A95
- Fouesneau, M. & Lançon, A. 2010, *A&A*, 521, A22
- Fouesneau, M., Lançon, A., Chandar, R., & Whitmore, B. C. 2012, *ApJ*, 750, 60
- Frostig, R., Johnson, M. J., & Leary, C. 2019, in *SysML Conference 2018*, Stanford, United States
- Golini, G., Montes, M., Carrasco, E. R., Román, J., & Trujillo, I. 2024, *A&A*, 684, A99
- Hahn, C. & Melchior, P. 2022, *ApJ*, 938, 11
- Hidalgo, S. L., Pietrinferni, A., Cassisi, S., et al. 2018, *ApJ*, 856, 125
- Iglesias-Navarro, P., Huertas-Company, M., Martín-Navarro, I., Knapen, J. H., & Pernet, E. 2024, *A&A*, 689, A58
- Iglesias-Navarro, P., Huertas-Company, M., Pérez-González, P., et al. 2025, *A&A*, 703, A229
- Ivezić, Ž., Kahn, S. M., Tyson, J. A., et al. 2019, *ApJ*, 873, 111
- Johnson, B. D., Leja, J., Conroy, C., & Speagle, J. S. 2021, *ApJS*, 254, 22
- Khim, D. J., Zaritsky, D., Sandoval Ascencio, L., Cooper, M. C., & Donnerstein, R. 2025, *ApJ*, 989, 154
- Kroupa, P. 2001, *MNRAS*, 322, 231
- Krumholz, M. R., Fumagalli, M., da Silva, R. L., Rendahl, T., & Parra, J. 2015, *MNRAS*, 452, 1447
- Kuntschner, H., Emsellem, E., Bacon, R., et al. 2010, *MNRAS*, 408, 97
- La Barbera, F., Vazdekis, A., Ferreras, I., et al. 2019, *MNRAS*, 489, 4090
- Leitherer, C., Schaerer, D., Goldader, J. D., et al. 1999, *ApJS*, 123, 3
- Li, D. D., Liu, Q., Eadie, G. M., et al. 2025, *ApJ*, 986, L18
- Maraston, C. 2005, *MNRAS*, 362, 799
- Martin, G., Bazkiaei, A. E., Spavone, M., et al. 2022, *MNRAS*, 513, 1459
- Martín-Navarro, I., Pinna, F., Coccato, L., et al. 2021, *A&A*, 654, A59
- Martín-Navarro, I. & Vazdekis, A. 2024, *A&A*, 691, L10
- Martínez-Delgado, D., Stein, M., Sakowska, J. D., et al. 2025, *A&A*, 701, A182
- McGaugh, S. S. & Schombert, J. M. 2014, *AJ*, 148, 77
- Mészáros, S., Bohlin, R., Allende Prieto, C., et al. 2024, *A&A*, 688, A197
- Mihos, J. C., Harding, P., Feldmeier, J. J., et al. 2017, *ApJ*, 834, 16
- Neumann, J., Fragkoudi, F., Pérez, I., et al. 2020, *A&A*, 637, A56
- Ocvirk, P., Pichon, C., Lançon, A., & Thiébaud, E. 2006, *MNRAS*, 365, 74
- Orozco-Duarte, R., Wofford, A., Vidal-García, A., et al. 2022, *MNRAS*, 509, 522
- Pelat, D. 1998, *MNRAS*, 299, 877
- Pickles, A. J. 1985, *ApJ*, 296, 340
- Pietrinferni, A., Hidalgo, S., Cassisi, S., et al. 2021, *ApJ*, 908, 102
- Pietrinferni, A., Salaris, M., Cassisi, S., et al. 2024, *MNRAS*, 527, 2065
- Pinna, F., Falcón-Barroso, J., Martig, M., et al. 2019, *A&A*, 623, A19
- Renzini, A. 1998, *AJ*, 115, 2459
- Robotham, A. S. G. & Bellstedt, S. 2025, *RAS Techniques and Instruments*, 4, rzaf019
- Rodríguez-Beltrán, P., Vazdekis, A., Cerviño, M., & Beasley, M. A. 2021, *MNRAS*, 507, 3005
- Roediger, J. C. & Courteau, S. 2015, *MNRAS*, 452, 3209
- Sánchez, S. F., Mejía-Narváez, A., Egorov, O. V., et al. 2025, *AJ*, 169, 52
- Sánchez-Blázquez, P., Peletier, R. F., Jiménez-Vicente, J., et al. 2006, *MNRAS*, 371, 703
- Schiavon, R. P. 2007, *ApJS*, 171, 146
- Schmidt, A. A., Copetti, M. V. F., Alloin, D., & Jablonka, P. 1991, *MNRAS*, 249, 766
- Spiniello, C., Trager, S., Koopmans, L. V. E., & Conroy, C. 2014, *MNRAS*, 438, 1483
- Spinrad, H. & Taylor, B. J. 1971, *ApJS*, 22, 445
- Stanway, E. R. & Eldridge, J. J. 2023, *MNRAS*, 522, 4430
- Strom, K. M. & Strom, S. E. 1978, *AJ*, 83, 73
- Thomas, D., Maraston, C., & Bender, R. 2003, *MNRAS*, 339, 897
- Thomas, D., Maraston, C., Bender, R., & Mendes de Oliveira, C. 2005, *ApJ*, 621, 673
- Tinsley, B. M. & Gunn, J. E. 1976, *ApJ*, 203, 52
- Tonry, J. & Schneider, D. P. 1988, *AJ*, 96, 807
- Tonry, J. L., Dressler, A., Blakeslee, J. P., et al. 2001, *ApJ*, 546, 681
- Trager, S. C., Worthey, G., Faber, S. M., Burstein, D., & Gonzalez, J. J. 1998, *ApJS*, 116, 1
- Trujillo, I., D’Onofrio, M., Zaritsky, D., et al. 2021, *A&A*, 654, A40
- Trujillo, I. & Fliri, J. 2016, *ApJ*, 823, 123
- van Dokkum, P. G., Abraham, R., Merritt, A., et al. 2015, *ApJ*, 798, L45
- Vazdekis, A., Casuso, E., Peletier, R. F., & Beckman, J. E. 1996, *ApJS*, 106, 307
- Vazdekis, A., Cerviño, M., Montes, M., Martín-Navarro, I., & Beasley, M. A. 2020, *MNRAS*, 493, 5131
- Vazdekis, A., Coelho, P., Cassisi, S., et al. 2015, *MNRAS*, 449, 1177
- Vazdekis, A., Sánchez-Blázquez, P., Falcón-Barroso, J., et al. 2010, *MNRAS*, 404, 1639
- Worthey, G. 1994, *ApJS*, 95, 107
- Worthey, G., Faber, S. M., & Gonzalez, J. J. 1992, *ApJ*, 398, 69
- Worthey, G., Faber, S. M., Gonzalez, J. J., & Burstein, D. 1994, *ApJS*, 94, 687
- Worthey, G. & Lee, H.-c. 2011, *ApJS*, 193, 1
- Zibetti, S., Charlot, S., & Rix, H.-W. 2009, *MNRAS*, 400, 1181

Appendix A: Young semi-resolved populations

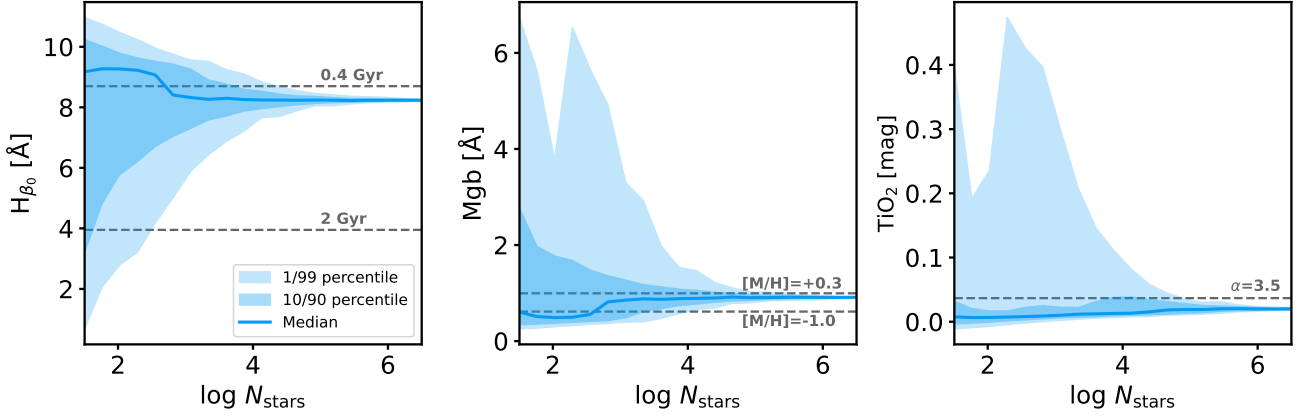


Fig. A.1. Same as Fig. 2 but the line-strength predictions have been calculated assuming a 0.25 Gyr old population.

Figures A.1 and A.2 replicate Figs. 2 and 5 from the main text but in this case for a young (0.25 Gyr) population, with solar metallicity and Milky Way-like IMF. Shaded contours indicate again the 1/99 and 10/90 percentiles of the distribution with a median value indicated by the solid line. Horizontal dashed lines in both cases mark the expected value for fully sampled SSP models with different ages, metallicities and/or IMF slopes.

The general behavior is similar as for old populations, with an evident increase in the scatter of the FASTAR predictions when the number of stars falls below $\log N_{\text{stars}} \lesssim 5$. However, the systematic biases in the colors and line-strengths are not the same as, for example, H_{β_0} tends to increase with decreasing number of stars. Moreover, the apparent lack of a systematic bias in these indices for a Milky Way-like IMF seeing for old populations does not hold true for younger ages.

In order to further exemplify the behavior of semi-resolved FASTAR predictions for younger ages, Fig. A.3 shows the age dependence of the H_{β_0} line for the three different $\log N_{\text{stars}}$ ranges ($\log N_{\text{stars}} = 2.5, 3.5$ and 5.5 , the same as in Fig. 4). These model predictions assume a Milky Way-like IMF. For clarity, we only include the distribution of the 1/99 percentiles, indicated with colored shaded areas, with the median value corresponding to the solid lines.

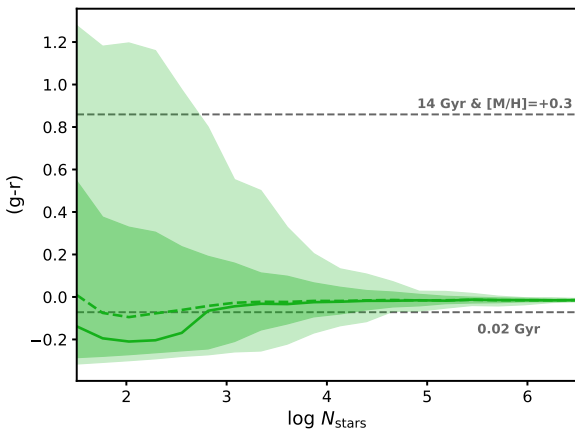


Fig. A.2: Same as Fig. A.2 but the $(g-r)$ color in this case corresponds to a younger (0.25 Gyr) stellar population.

In general, the behavior is similar for the three $\log N_{\text{stars}}$ values, although there are clear systematics. For younger ages, low $\log N_{\text{stars}}$ values tend to correspond to stronger H_{β_0} values, while for older ages the trend is reversed. The bottom panel of Fig. A.3 highlights these systematic differences showing the residuals with respect to the fully sampled FASTAR predictions. It is worth emphasizing that these systematic differences result from the biased sampling of specific stellar evolutionary phases, i.e., different stellar masses, and thus they are modulated by the assumed IMF.

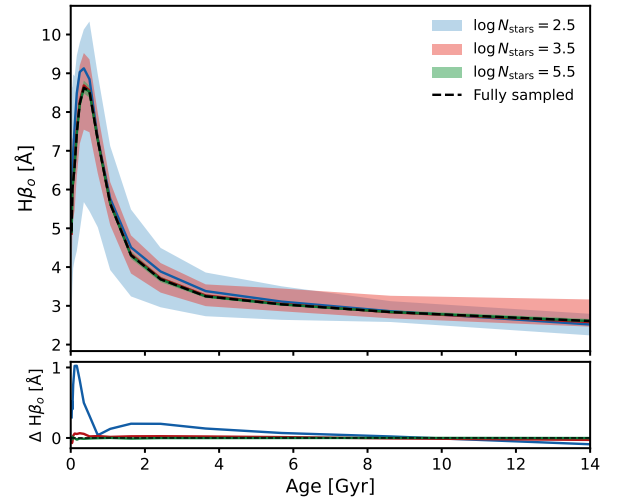


Fig. A.3: Age dependence of H_{β_0} . The top panel shows the distribution FASTAR H_{β_0} predictions as a function of age, for three different $\log N_{\text{stars}}$ values: 2.5 in blue, 3.5 in red and 5.5 in green. The shaded areas correspond to the 1/99 percentiles and the solid colored lines to the median trend. For reference, the predicted trend for a fully sampled population is shown with a dashed black line. The bottom panel shows the residuals between this dashed black lines and each of the median trends.